JGR Solid Earth

RESEARCH ARTICLE
10.1029/2024JB028763

Permeability Anisotropy in Brittle Carbonate Fault Rocks

E. A. H. Michie[1] and I. Kaminskaite-Baranauskiene[2]

[1]University of Liverpool, Liverpool, UK, [2]Faculty of Chemistry and Geoscience, Vilnius University, Vilnius, Lithuania

Key Points:

- A notable permeability anisotropy is documented in carbonate fault rocks, where the lowest permeability generally occurs across-fault
- The cause of permeability anisotropy varies with lithofacies/host porosity and juxtaposition
- The permeability anisotropy is caused by Riedel shears in low porosity carbonates and elongated pores in high porosity carbonates

Supporting Information:

Supporting Information may be found in the online version of this article.

Correspondence to:

E. A. H. Michie,
emma.michie@liverpool.ac.uk

Citation:

Michie, E. A. H., & Kaminskaite-Baranauskiene, I. (2025). Permeability anisotropy in brittle carbonate fault rocks. *Journal of Geophysical Research: Solid Earth*, *130*, e2024JB028763. https://doi.org/10.1029/2024JB028763

Received 17 JAN 2024
Accepted 25 FEB 2025

Author Contributions:

Conceptualization: E. A. H. Michie
Formal analysis: E. A. H. Michie, I. Kaminskaite-Baranauskiene
Investigation: E. A. H. Michie
Methodology: E. A. H. Michie, I. Kaminskaite-Baranauskiene
Resources: E. A. H. Michie
Validation: E. A. H. Michie, I. Kaminskaite-Baranauskiene
Visualization: E. A. H. Michie
Writing – original draft: E. A. H. Michie
Writing – review & editing: E. A. H. Michie, I. Kaminskaite-Baranauskiene

Abstract

Permeability anisotropy of fault rocks has been documented in crystalline and clastic lithologies, but rarely within carbonates. In this contribution, we investigate how a permeability anisotropy may develop within carbonate fault rocks, including deformation bands, for the purpose of improving understanding of fluid flow. A total of 43 oriented fault rock samples plugged in three orthogonal directions were taken from eight faults in differing carbonate lithofacies. The permeability was measured, with the goal of assessing if and to what extent a permeability anisotropy may develop. Key factors controlling the formation of anisotropy in these rocks were analyzed by combining petrophysical and microstructural data. All samples showed some degree of anisotropy. However, a consistent major permeability anisotropy (up to five orders of magnitude) only occurred when the same or similar lithofacies were juxtaposed, where the lowest permeability was recorded normal to fault strike in 75% of the samples. Differences occurred in the highest permeability direction dependent on lithofacies. In deformation bands within high porosity grainstones, the highest permeability was inferred to be at a low angle to σ_1, created by grain and pore alignment in the direction of transport. The highest permeability in faults cutting recrystallized carbonates varied from sub-parallel to σ_1, to sub-parallel to σ_2, owing to variations in Riedel shears and fracture orientation during multiple reactivation episodes. Predicting the permeability of a fault zone, including any directional permeability, is key for improved modeling of fluid flow pathways around faults in the subsurface.

Plain Language Summary

The permeability of rocks can be directionally dependent, known as a permeability anisotropy. A permeability anisotropy has previously been documented in unfaulted and faulted rocks across a range of lithologies. However, permeability anisotropy has rarely been documented in carbonate fault rocks. This contribution documents a unique dataset of permeability anisotropy in fault rock from a range of carbonate lithofacies along with describing the conditions in which a permeability anisotropy may develop. Specifically, in faulted high porosity carbonates, the pore network is elongated along the direction of fault movement, such that flow is enhanced in this orientation, but lowered perpendicular. Faulting in low porosity carbonates creates localized fine-grained zones and fractures that prevent flow across the fault but enhance flow along or down the fault. However, no systematic permeability anisotropy is created in fault rocks when two different carbonate lithofacies are offset, such that the lowest or highest permeability can occur in any orientation. This can be attributed to a variety of deformation and diagenetic mechanisms at play along fault-strike. Knowing when a permeability anisotropy may be created along a fault slip surface, and to what extent, is crucial for fluid flow modeling in the subsurface.

1. Introduction

Faults are inherently heterogeneous at a range of scales, with strain distributed throughout the fault zone as either low strain structures forming the "damage zone (DZ)" (the outermost zone), or as high strain "fault rock" formed within the "fault core" (the innermost zone) that is generally localized along a slip surface (Caine et al., 1996; Chester & Logan, 1986). Beyond the DZ is the host rock, where no strain from nearby faulting has occurred. Fracturing is common within DZs (e.g., Kim et al., 2004), along with deformation bands that can form in high-porosity rocks (e.g., Qu and Tveranger, 2016; Schueller et al., 2013). Brittle fault rock can vary due to stress accommodation or associated with lithologies displaced, and can be classified as fault gouge, cataclastic or brecciated (Sibson, 1977).

The complex internal structure of fault zones leads to faults that often play an important role in influencing fluid flow within the subsurface (e.g., Antonellini & Aydin, 1994; Bense & Person, 2006; Faulkner et al., 2010; Knipe et al., 1998; Sibson, 1994). Hence, understanding any permeability anisotropy created along the slip surfaces will improve our ability to accurately predict fault hydraulic behavior in the subsurface (e.g., Bense & Person, 2006), such as flow pathway direction.

A permeability anisotropy has previously been recorded in carbonate host rocks, varying up to two orders of magnitude, but more commonly less than 1, associated with variations in lithofacies (Nabawy, 2018; Sahin et al., 2007; Sun et al., 2017; Widarsono et al., 2006). High porosity granular lithofacies show a higher degree of homogeneity, and are generally considered isotropic, whereas muddy, lower porosity lithofacies show a subtle permeability anisotropy where vertical permeability is lower than the horizontal (Sahin et al., 2007).

A permeability anisotropy is also recorded in faulted lithologies; either as a localized permeability anisotropy within the fault core, or as a bulk permeability anisotropy considering the hydraulic conductivity of the whole fault zone. Specifically, permeability can be modified by fault-related processes such as fracturing and dissolution within the damage zone that act to increase the permeability, allowing fluids to flow along-strike and up fault dip (e.g., Agosta et al., 2010; Aydin, 2000; Evans et al., 1997; Ferrill & Morris, 2003; Smeraglia et al., 2021). Conversely, processes such as cataclastic flow, diagenesis and clay smearing within the fault core often causes a reduction in permeability, restricting fluid flow within and across a fault (Ballas et al., 2015; Crawford, 1998; Cuisiat & Skurtveit, 2010; Fisher & Knipe, 1998; Flodin et al., 2005; Kaminskaite et al., 2019; Kettermann et al., 2020; Vrolijk et al., 2016). As such, a fault zone itself is considered to have a bulk structural permeability anisotropy (Antonellini & Aydin, 1994; Caine et al., 1996; Evans et al., 1997; Flodin et al., 2001; Seeburger, 1981).

In addition to the bulk anisotropy, the deformed fault rock localized on slip surfaces can also show a permeability anisotropy, which is the focus of this study. Modeling any preferred permeability pathways created by a permeability anisotropy within the fault core is important for fault seal analysis, particularly along-fault flow (Bjørnarå et al., 2023). Further, understanding pore shape variations creating a permeability anisotropy may aid predictions of fault stability (Healy, 2009, 2012). Studies have documented a permeability anisotropy in fault rock (Cavailhes et al., 2013; Farrell et al., 2014), gouge (Arch & Maltman, 1990; Evans et al., 1997; Faulkner & Rutter, 1998; Kopf, 2001; Wibberley and Shimamoto, 2005), or catalcastic deformation bands (e.g., Antonellini & Aydin, 1994). In many cases, permeability has been shown to be lower perpendicular to the fault plane, compared to parallel.

Experimental methods have previously identified a permeability anisotropy in synthetic fault rock gouge, where permeability is shown to be approximately one order of magnitude lower perpendicular to fault-strike than parallel (Sato et al., 2018; Zhang et al., 1999; Zhang & Tullis, 1998). Zhang & Tullis (1998) documented layering of fine-grained particles in pure quartz gouge, that also contained *Y*-shears that allowed flow parallel to the slip plane but impede flow across it. Image analysis and calculations of permeability of deformation bands has also shown a permeability anisotropy, where the permeability perpendicular to the deformation band is calculated to be lower than parallel (Torabi et al., 2008). Permeability anisotropy has also been widely recorded in laboratory measurements of outcropping fault rock samples, where permeability is typically lower perpendicular to fault strike (Antonellini & Aydin, 1994; Cavailhes et al., 2013; Evans et al., 1997; Farrell et al., 2014; Faulkner & Rutter, 1998; Shipton et al., 2002; Torabi et al., 2021; Wibberley & Shimamoto, 2005). Variations in permeability orientation can reach up to five orders of magnitude in high-porosity sandstone faults due to compaction and shearing that create elongated pores (Farrell et al., 2014).

Although studies have shown permeability anisotropy developed in fault rock within crystalline (Evans et al., 1997), clay-rich (Arch & Maltman, 1990; Faulkner & Rutter, 1998; Wibberley and Shimamoto, 2005), quartz-feldspathic and micaceous material (Zhang et al., 1999), and quartz-rich material (Farrell et al., 2014; Zhang & Tullis, 1998), there are limited documentations of a notable permeability anisotropy in faulted carbonates (Ferraro et al., 2020, who documented permeability varying less than an order of magnitude between orientations). Despite significant advancements in understanding fault-related permeability anisotropy, no systematic studies have yet explored its development across varying carbonate lithofacies, the mechanisms controlling its formation, or its extent. In this study, we focus on identifying the conditions under which permeability anisotropy may (or may not) develop exclusively within carbonate fault rocks, including deformation bands. Our goal is to investigate and elucidate the factors that drive anisotropy in fault rocks formed within diverse carbonate lithofacies. This analysis will provide critical insights to refine subsurface fluid flow models and enhance predictions of reservoir behavior in carbonate-dominated systems.

2. Geological Background

This study draws on data collected from eight fault zones located in Italy and Malta (Figures 1a and 1b; Table S4 in Supporting Information S1). These faults traverse a range of carbonate lithofacies (Figures 1c–1g), each with

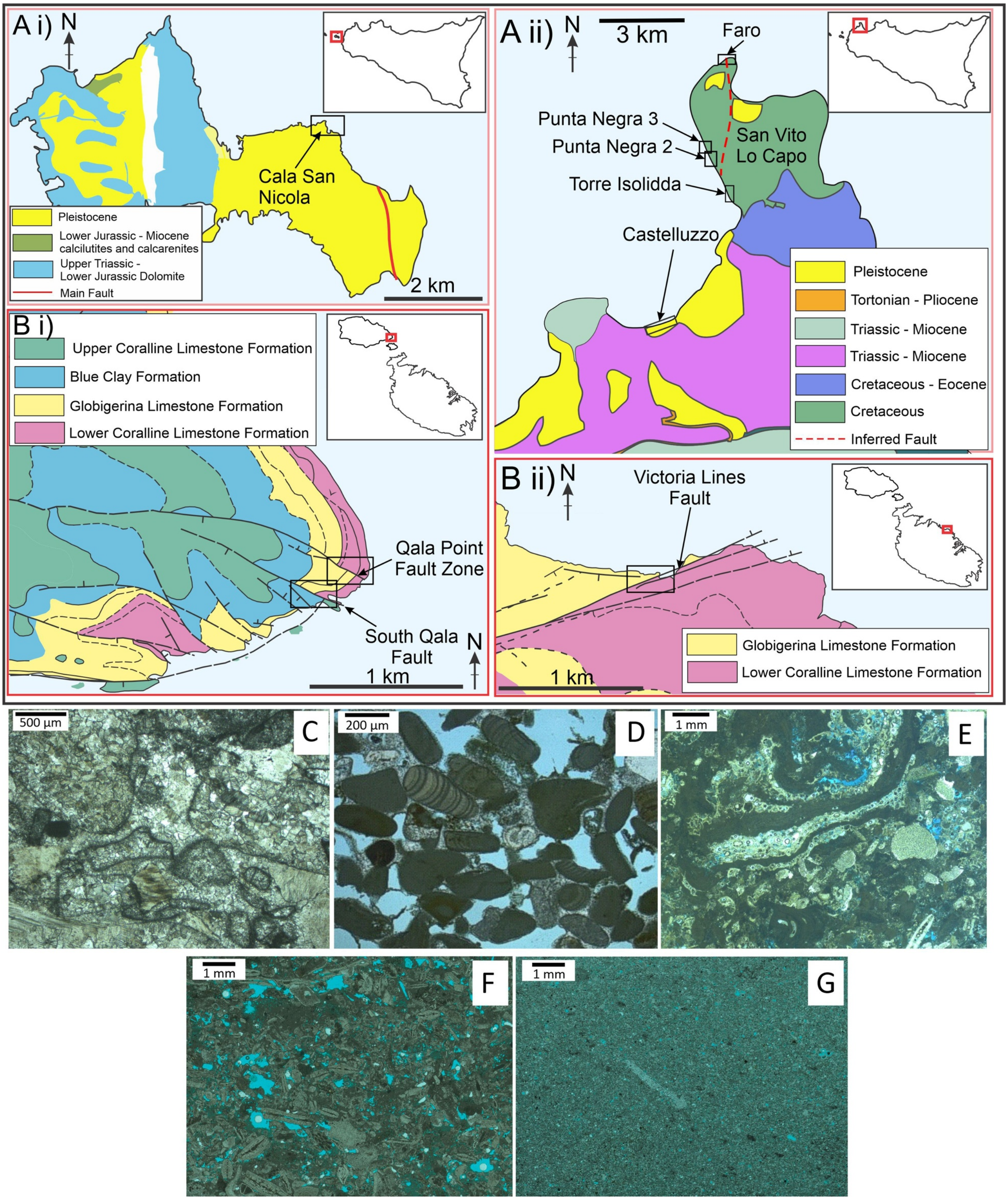

Figure 1. Localities of the two main study areas: (a) Sicily, and (b) Malta (a i) Simplified geological map of Favignana modified after Abate et al. (1997) (a ii) Simplified geological map of San Vito lo Capo modified after Abate (1993) (b i) Geological map of SE Gozo (Continental Shelf Department Malta, 2022) (b ii) Geological map of East Malta (Continental Shelf Department Malta, 2022). One main locality has been studied on the Island of Favignana: Cala San Nicola to the East of the Island (a i). Five localities have been studied on mainland Sicily: Faro Fault, Punta Negra Faults and Torre Isolidda Fault, and nearby Castelluzzo coast (a ii). Recrystallized carbonates are studied on the San Vito Lo Capo peninsula, whilst deformation bands have been studied at the Castelluzzo coast and the Island of Favignana. Three faults have been studied at two main localities on the Maltese Islands: the Victoria Lines Fault, east coast Malta, and Qala Point Fault Zone and South Qala Fault, south-east Gozo (b). Example host rock textures are shown: (c) recrystallized carbonates, Sicily, (d) high porosity grainstones, Sicily, (e) algal-rich packstones, Malta, (f) bioclastic packstones, Malta, and (g) wackestones, Malta.

distinct host rock porosities and permeabilities. This diversity allows us to evaluate the factors influencing the development and magnitude of permeability anisotropy within fault rocks formed in various carbonate settings. While the sites have complex and differing tectonic histories, which might complicate direct comparisons, our analysis focusses on permeability anisotropy at the sample level. By aggregating data from the same locality, we mitigate these complications, enabling robust insights into the processes driving anisotropy in faulted carbonates.

2.1. NW Sicily, Italy

NW Sicily is located on the western edge of the Sicilian-Maghrebian fold-thrust belt, composed of south-verging folds and thrusts, which formed during the Cenozoic collision between the North-African margin and Sardinia-Corsica block. The faults have gone through E-W trending thrust tectonics in the Early Miocene, extensional tectonics from the Late Miocene, followed by strike slip events within the Plio-Pleistocene (Catalano et al., 1985; Giunta et al., 2000; Tondi et al., 2006).

Four main faults have been studied on NW Sicily, Italy (Figure 1a). These faults are located around the San Vito Lo Capo peninsula; Faro, Torre Isolidda and two in Punta Negra (see Kaminskaite et al., 2020; Michie, Kaminskaite, et al., 2021; Michie et al., 2024 for further locality details; Figure 1Aii). All four studied faults show displacements of up to 10's meters, but with precise displacement hard to determine due to lack of marker beds. They show predominantly strike-slip kinematic, with minor (<20 m) normal offset (Kaminskaite et al., 2020). Maximum burial depth is around 2,000 m, with depth at time of strike slip faulting estimated as 200 m (Kaminskaite et al., 2020; Stead, 2018). All faults show localized deformation, with a single fault core surrounded by a damage zone. An example of fault exposure and characteristics is shown in Figure 2a. The fault rocks show dolomitization or have been resealed by calcite cementation after brecciation. The dolomitized fault rocks were reactivated during the Plio-Pleistocene event, forming polyphase breccias (Kaminskaite et al., 2020). All studied faults on San Vito Lo Capo Peninsula, NW Sicily cut low porosity (<2%) recrystallized packstones of Cretaceous age (Figure 1c). Since these faults juxtapose only low porosity recrystallized carbonates, we refer to these faults as similar juxtaposition types.

Low displacement (millimeters to a few centimeters) faults in highly porous granular rocks, commonly referred to as "deformation bands", have also been studied in NW Sicily, on the Island of Favignana (Figure 1a i), and along the Castelluzzo coast (Figure 1a ii) (see Kaminskaite et al., 2019; Michie et al., 2024 for further locality details). Deformation bands generally do not show significant offset, but instead form single bands that may localize into complex structures containing zones of anastomosing bands known as clustered deformation bands. Clustered bands represent a mature stage in the evolution of faults, acting as precursors to through-going faults with notable offset (Fossen et al., 2007; Tondi et al., 2012). The studied deformation bands are considered clustered bands (example of deformation band characteristics and exposure shown in Figure 2b). These deformation bands cut high porosity (*c*.47%) Upper Pliocene-Lower Pleistocene bioclastic grainstones and have been shallowly buried to *c*.50 m (Abate et al., 1997; Kaminskaite et al., 2019, Figure 1d). The deformation bands show right-lateral strike-slip kinematics for the E-W and ESE-striking bands, left-lateral strike-slip kinematics for the NNW and N–S trending bands, and oblique normal kinematics for NW-striking bands (Tondi et al., 2006). Four deformation bands are analyzed in this contribution; one from a band trending NW–bW, with kinematics predominantly showing oblique slip, two from bands trending WNW-ESE, with right-lateral strike slip kinematics, and one from a band rending roughly N–S, with left-lateral strike slip kinematics. Since there is negligible offset produced in deformation bands, we refer to these as self-juxtaposition.

2.2. Malta

Three fault zones have been studied in Malta (Figure 1b): one on the Island of Malta (Victoria Lines Fault; Figures 1b ii and 2c) a nd two on the Island of Gozo (Qala Point Fault and South Qala Fault; Figure 1b i). The faults formed during the Pliocene-Quaternary as part of the transtensional system in the foreland of the Sicilian-Apennine-Maghrabian fold-thrust belt. This transtensional system formed two main fault trends: NW–SE and ENE-WSW (Dart et al., 1993; Pedley et al., 1976). The studied faults trend ENE-WSW, with some curvature observed at the Qala Point Fault, where the fault trend shifts to NW–SE, showing an undetermined amount of strike slip accommodation. All faults show normal kinematics, with fault displacements ranging from *c*.30 m at Qala Point Fault, *c*.50 m at South Qala Fault (Cooke et al., 2018) and *c*.90 m at Victoria Lines Fault (Michie et al., 2014).

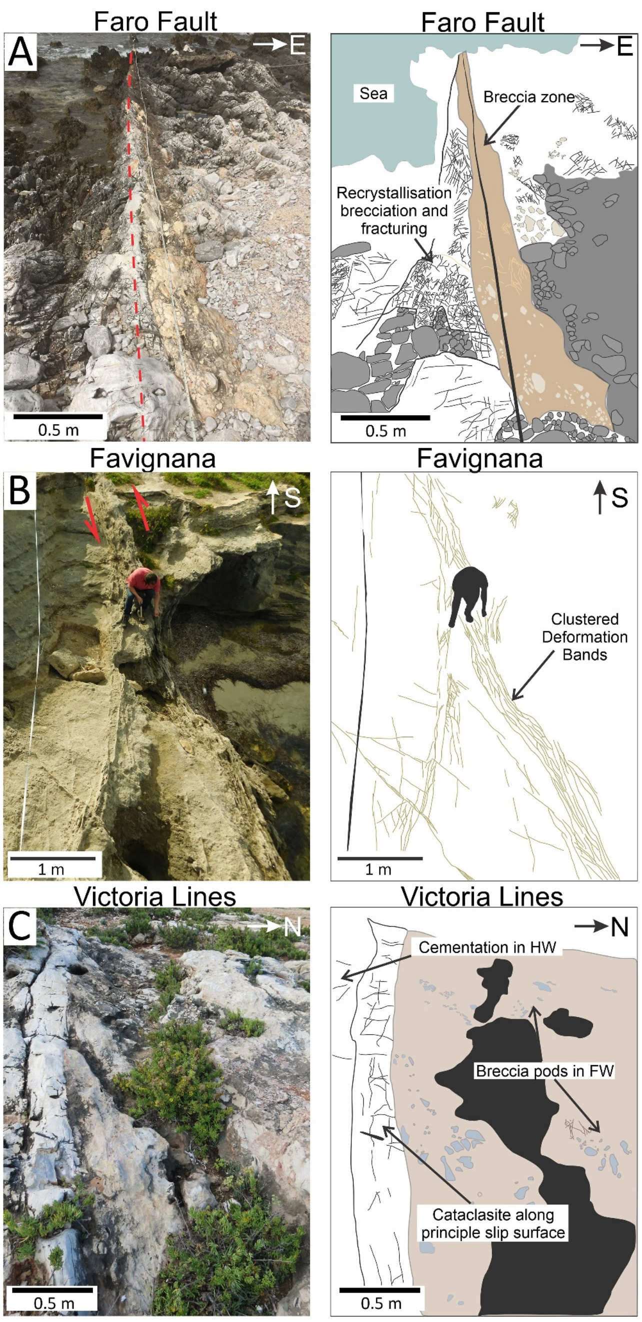

Figure 2. Example outcrop exposures of some of the main faults studied. (a) Faro Fault. 1 principal slip surface, dashed red line, with localized high intensity brecciation surrounded by fractured recrystallized rock with some lower intensity brecciation, (b) Clustered deformation bands, Favignana showing left lateral kinematics, at location of sample Si052, and (c) Principal slip surface of the Victoria Lines Fault, showing a wide cataclastic zone surrounded by brecciation. This fault zone extends a significant distance to the north.

The Qala Point Fault shows a complex zone of fracturing and subsidiary slip surfaces and numerous fault strands that host offset. Several right-stepping pull-apart structures are apparent within the overall fault zone, which contain Riedel shear surfaces with minor offset and an increased fracture density (Cooke et al., 2018). The South Qala Fault is a relatively simple fault zone, with 2 well-exposed slip surfaces that form a right stepping relay zone, with a fault bridge between. The slip surface shows a polished appearance, and occurs with several fault splays, parallel slip surfaces and lenses of intensely fractured and brecciated rock. An increased fracture density is observed within the damage zone, where the fractures are open (Cooke et al., 2018). The Victoria Lines Fault shows

10.1029/2024JB028763

a principal slip surface where the main offset has accumulated, with varying fault rock types observed along fault-strike, with cataclasite and a variety of breccias prevalent (Figure 2c). Multiple slip surfaces are observed, extending some 10's m into the hanging wall, in combination with a high fracture density (Michie et al., 2014).

The faults cut a variety of carbonate lithofacies, of Oligocene to Miocene age, from algal packstones (Attard Member; Figure 1e) and bioclastic packstones (Xlendi Member; Figure 1f) of the Lower Coralline Limestone Formation (LCL) to wackestones of the Lower Globigerina Limestone Formation (LGL; Figure 1g) (Dart et al., 1993; Pedley et al., 1976). The Blue Clay Formation (BC) is also observed within the faulted succession; a carbonate-rich clay, that is, a marl. These lithofacies have varying host porosities and permeabilities. The Attard Member has average porosities of 10%–15% and permeabilities of c.1 mD; Xlendi Member has average porosities of 20%–35% and permeabilities of 50–200 mD; Globigerina Limestone Formation has average porosities of 25%–36% and permeabilities of 2–25 mD (Michie & Haines, 2016; Michie, Cooke, et al., 2021). The succession has been shallowly buried to depths of 200–1,000 m (Bonson et al., 2007; Cooke et al., 2018; Dart et al., 1993; Kim et al., 2003; Michie & Haines, 2016). All fault zones offset different lithofacies. Hence, we refer to these faults as juxtaposition of different lithofacies.

3. Methodology

Forty-three oriented fault rock samples, each cobble-sized, were collected using a hammer and chisel for detailed analysis of matrix permeability anisotropy and its associated microstructures. Four are from different deformation bands, NW Sicily, three along-strike Punta Negra 2, five along-strike Punta Negra 3, eight along-strike Torre Isolissa, four along-strike Faro Fault, NW Sicily, two along-strike South Qala Fault, nine along-strike Qala Point Fault, and eight along-strike Victoria Lines Fault, Malta. See Michie, Cooke, et al. (2021) and Michie, Kaminskaite, et al. (2021) for precise sample localities. Where possible, each sample has been cored in three orientations: *x*: fault parallel, along fault-strike, *y*: fault parallel, down fault-dip, and *z*: perpendicular to fault-strike (Figure 3), with core plugs containing 100% fault rock material. Further, 10 oriented host samples have been collected: two from the Attard Mb, Xlendi Mb and LGL Mb on Malta, two from the grainstones on NW Sicily, and three from recrystallized host rocks on NW Sicily. Host rocks have also been cored in three orthogonal directions where possible: *x* and *y*: parallel to bedding at 90°, and *z*: perpendicular to bedding (Figure 3). In total, one hundred twenty-nine fault rock core plugs, and 28 host rock core plugs have been measured. Each core plug is 1–1.5 inch in diameter. Fifty-seven thin sections have also been made in these three orientations. Thin sections were taken adjacent to the representative core plugs, to accurately capture the microstructures representing the measured petrophysical properties (Figure 3).

3.1. Permeability Measurements

Permeability measurements have been made on all one hundred and fifty-seven 1–1.5 inch core plugs (see Michie et al., 2024 for data). These core plugs were cleaned to remove salts using deionized water saturated with carbonate sediment of the same composition as the sample. They were then dried at 60°C to prevent damage to any clay content, continuing until their weight stabilized, which typically took between 3 and 7 days (American Petroleum Institute, 1998).

Single-phase gas permeability measurements were acquired using either a steady-state Jones Nitrogen Permeameter at the Aberdeen Petrophysical Laboratory (Maltese samples) and CoreLab 200 helium PDP pulse-decay permeameter at the Wolfson Multiphase Flow laboratory (Sicilian samples). Laboratories maintained a temperature-controlled environment, ±0.5°C. The CoreLab 200 system is adapted to perform both steady-state and pulse-decay methods for high (>0.1 mD) and low (<0.1 mD) permeability samples, respectively. Samples from the same locality were analyzed using the same apparatus.

To investigate properties at geologically accurate subsurface conditions, and provide a realistic understanding of fault behavior under fault-induced stress conditions, confining pressures equivalent to the estimated depth at time of faulting were applied using:

$$\mathrm{Pc} = \rho \mathrm{gh}$$

where Pc is the confining pressure (Pa), ρ is density of the formation (kg/m3), g is gravitational force (9.80665 m/s2), and h is burial depth of the sample at the estimated depth at time of faulting (m). Confining pressures

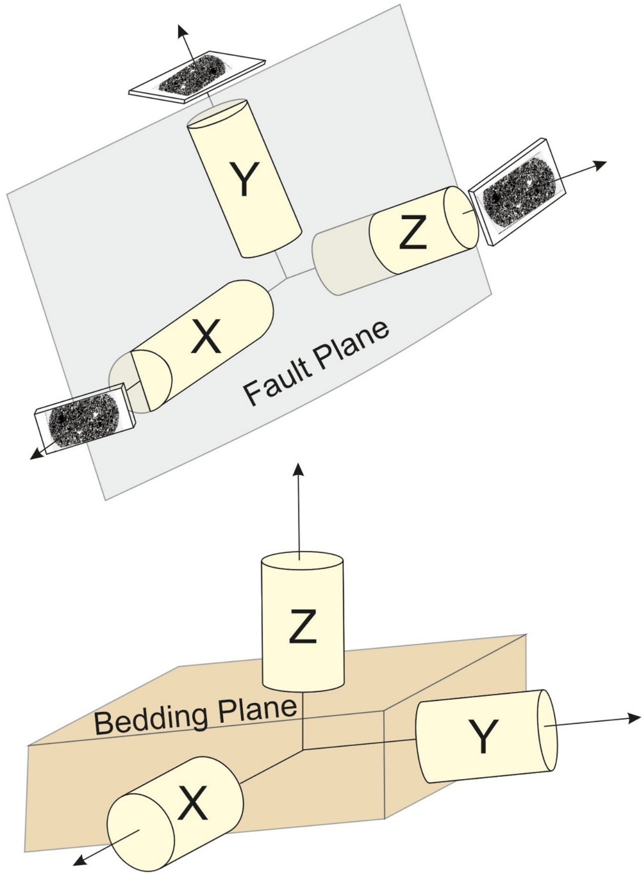

Figure 3. Orientation of core plugs and thin sections with respect to the fault surface (for fault rock samples, top) and bedding planes (for host samples, bottom).

equivalent of maximum depth at time of faulting reduces the influence of fracturing due to uplift and relaxation or sample retrieval (2.8–20.7 MPa).

For pulse-decay permeability tests using the CoreLab 200 PDP, measuring low (<0.1 mD) permeability samples, the pore pressure was increased and allowed to equilibrate across the sample (varying roughly 2.8–7 Mpa), after which a differential pressure was introduced and both the absolute and differential pore pressures were monitored until the pressure re-equilibrated. Permeability was calculated using the methods of Jones (1997) according to Darcy's Law. For steady-state tests using the CoreLab 200 PDP, measuring high (>0.1 mD) permeability samples, a constant upstream pressure was applied while the downstream was vented through a flowmeter. The differential pressure across the sample was monitored until it stabilized, where the flow rate and differential pressure were recorded to calculate permeability using an adaption of Darcy's Law that accounted for the gas compressibility:

$$Kg = 2000\mu \frac{L}{A} \frac{V}{t} \frac{P_{atm}}{\left(P_1^2 - P_2^2\right)}$$

Where Kg is the gas permeability (mD), μ is gas viscosity (cP), L is plug length (cm), A is plug cross section are (cm^2), V is volume of fluid passed in t seconds at ambient conditions measured at the outlet (cm^3), t is time (seconds), P_{atm} is atmospheric pressure (atm absolute = 1), P_1 is upstream pressure (atm absolute) and P_2 is downstream pressure (atm absolute).

This equation accounts for gas compressibility by using the squared pressure difference term, which corrects for gas expansion effects.

Steady-state permeabilities using the Jones Nitrogen Permeameter allowed for flow rates to be measured by two techniques, depending on their magnitude. The built-in flowmeter technique was used to measure flow rates >0.025 ml/s, while the traveling meniscus flowmeter was used to measure flow rates between 0.0001–0.025 ml/s. Permeability was then calculated according to Darcy's law using flow rates measured.

Measuring permeability by using gas results in gas slip on the pore walls that creates a deviation from the continuum flow, known as the Klinkenberg effect. Gas slippage results in a decrease in the measured gas permeability as the mean gas pressure increases. To correct for this, a linear regression of the apparent permeability with the reciprocal of the mean pore pressure, $1/P$, was plotted using several mean gas pressures (≥4 data points; See Supporting Information S1 data for permeability examples from the different techniques). The intercept on the permeability axis gives the Klinkenberg corrected permeability (Klinkenberg, 1941).

3.2. Microscopy and Micro-CT Analysis

Optical microscopy and scanning electron microscope-backscatter electron microscopy has been used to analyze the main deformation and/or diagenetic microstructures within each perpendicular fault rock thin section to provide an overview of the deformation history of the outcrops and to identify potential cause(s) for a permeability anisotropy developed. The thin sections were impregnated with blue epoxy under vacuum, infilling the porosity, to aid with pore space identification and quantification (Grove & Jerram, 2011).

X-ray computer tomography data from three orthogonal core plugs from deformation bands have been taken to assess pore orientation in 3D space. Samples were scanned with a Zeiss Xradia Versa 620 *X*-ray microscope. A source accelerating voltage of 160 kV at 25 W was used, and the beam filtered with a HE4 beam filter. The 0.4*X* objective was chosen, and the field of view adjusted to 42 × 42 mm, which resulted in a voxel size of 21 μm (detector binning 1), a resolution that allows for macro-pores to be detected and analyzed on full core plugs. For each scan, 3,201 projection images with an exposure time of 21 s each were collected over 360° and reconstructed with Zeiss proprietary software Scout-and-Scan Reconstructor version 16.1.

3.2.1. Image Analysis

Full thin section scans have been acquired using a Microscopes International uScopeGX scanner, at 10× resolution. Scans were imported into ImageJ (Rasband, 2018), which have then been converted to 8-bit images, threshold to isolate key features and then used to quantify the main orientation data of shears and pores (see Michie et al., 2024 for supplementary data).

To assess the orientation of the Riedel shears, we have used full thin section scans to perform image analysis, thresholding only these shears, where one pixel is 3 μm. Median filtering to remove <2 pixel in size was first performed, to reduce noise. Thresholding was performed to isolate the shears. Due to their fine-grained nature, these have a relatively uniform, darker appearance than the surrounding rock matrix allowing for isolation. The isolated shears were then analyzed using best-fit ellipses. We assessed whether there is any preferred orientation to the shears by examining the angle of the ellipses. However, the quantity of minor shears or dense features dominated the results, with the largest shears summarized in only a couple of points. This meant the largest shears do not show up as a significant influence on the overall preferred orientation. To mitigate against this, the area weighted percentage has been taken, with any shears <0.01 mm^2 being removed. The frequencies are then normalized to compare between.

To quantify pore elongation, we have used image analysis on three orthogonal 2D thin sections (see Figure 3 for orientation details), and on 3D micro-CT scans (see Michie et al., 2024 for supplementary data), where one pixel is 21 μm. For the 2D image analysis, ImageJ was used to isolate the pores within each thin section, after filtering using a median algorithm removing those with <2 pixel in size. Pores were isolated using visualization of the blue dye. A best-fit ellipse was applied to the pores, and the angle of the longest axis was measured from the x-plane. For 3D images from MicroCT scans, a 3D median filtering of two pixels was applied, pores were thresholded, then labeled using the Morpholibj plugin (Legland et al., 2016). The labels were filtered based on size, where <500 voxels were removed for clarity and computation space. Ellipsoids were applied to each pore label, and their 3D angles were recorded.

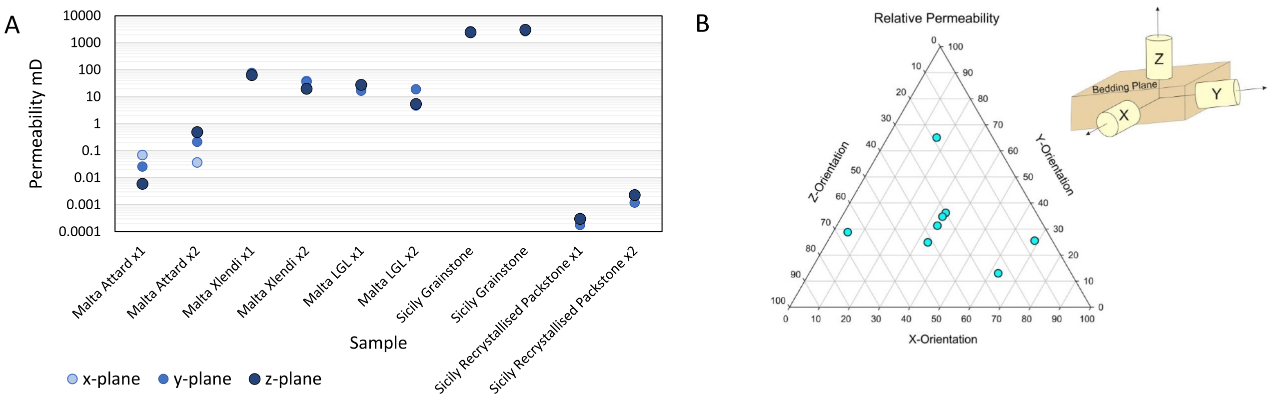

Figure 4. (a) Permeability data from representative host samples in X, Y and Z orientations. Note that not all samples have core plugs taken in three orthogonal orientations. (b) Relative proportion of permeability in the 3 orientations. The samples show no systematic permeability anisotropy, with permeabilities generally varying over one order of magnitude or less, representative of inherent heterogeneity. Names of samples relate to their fault rock counterparts; Malta (all Maltese faults), Sicily Grainstones (deformation bands) and Sicily recrystallized packstone (San Vito Lo Capo faults).

4. Results

4.1. Permeability of Host Samples

Before evaluating whether permeability anisotropy exists for fault core samples, it is essential to first determine if any permeability anisotropy is present in the host rock, as this may influence the fault core results. In all host rock samples, no significant permeability anisotropy is observed (Figures 4c and 4d). While subtle variations exist, they are generally less than one order of magnitude between orientations. The largest recorded variation, up to one order of magnitude, occurs within the algal packstones of Malta (Attard Mb). However, this permeability anisotropy is not systematic, as the *z* orientation records both the highest and lowest permeability values across two samples. Further, the permeability variation between these two samples exceeds two orders of magnitude, suggesting that this variability is a product of inherent lithofacies heterogeneity and the proportion of algal matter present. As such, the host rock can be considered isotropic, and any permeability anisotropy observed within fault core samples must be the attributed to deformation mechanisms associated with faulting.

4.2. Fault Core Permeability Anisotropy

While a permeability anisotropy is present in all fault rock samples, only certain faults exhibit a consistent pattern of anisotropy (Figure 5). A key factor influencing whether a systematic permeability anisotropy occurs appears to be juxtaposition type and the resulting heterogeneity. When similar lithofacies are juxtaposed, or when self-juxtaposition occurs (such as deformation bands), a systematic permeability anisotropy is observed (Figure 5). Conversely, when different lithofacies are juxtaposed, no systematic permeability anisotropy is recorded, and the lowest and highest permeability can occur in any core plug orientation.

In this study, we categorize the results according to juxtaposed lithofacies, including host porosity. Specifically, we distinguish between deformation bands found in high porosity grainstones and larger faults offsetting low porosity recrystallized packstones.

4.2.1. Juxtaposition of Self/Similar Lithofacies

4.2.1.1. Recrystallized Carbonates

When self or similar low porosity recrystallized carbonate lithofacies are juxtaposed, a systematic permeability anisotropy is observed. The lowest permeability is generally within the z-oriented plugs (perpendicular to slip surface), although some scatter can occur. The highest fault core permeability values are observed equally

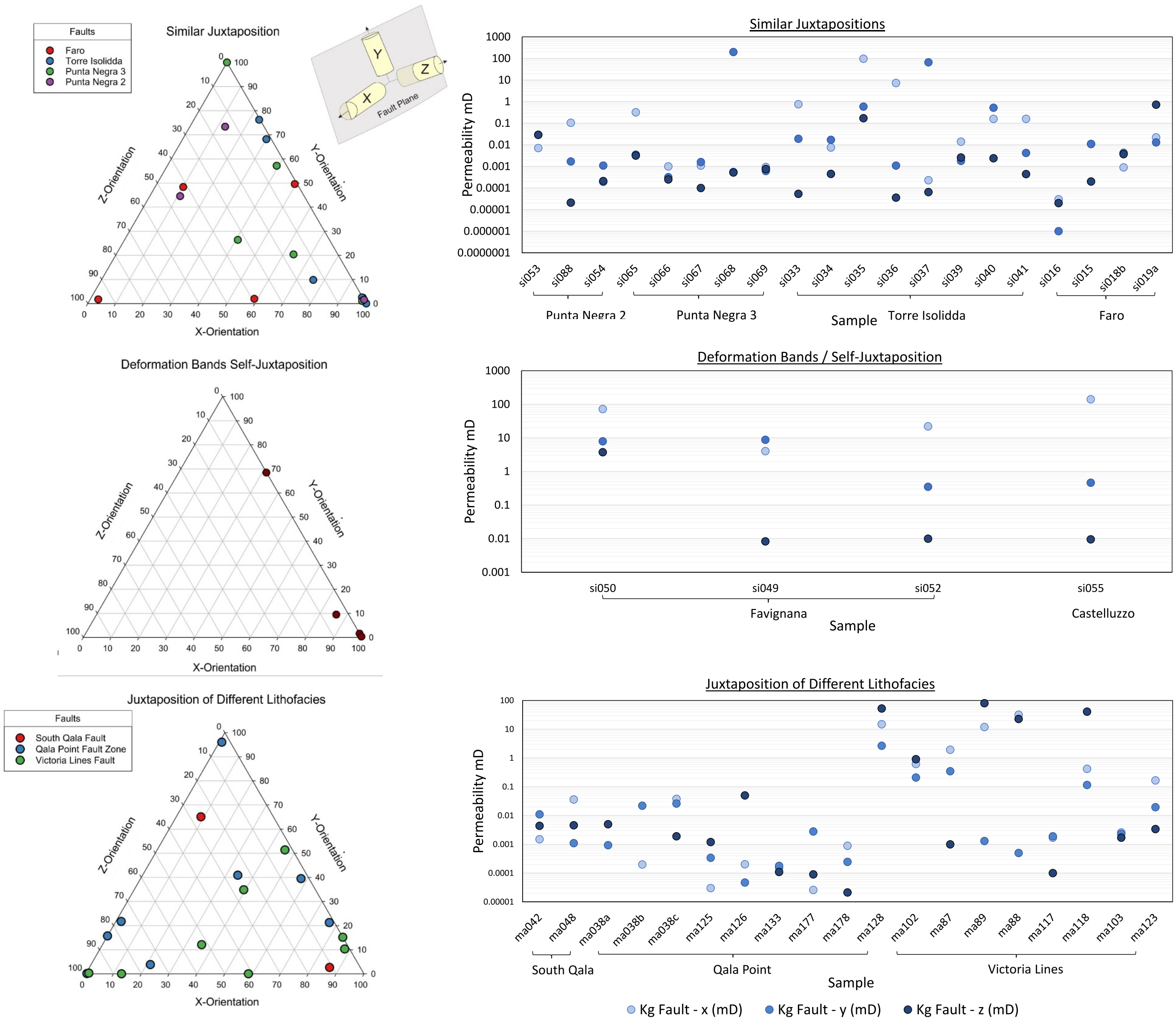

Figure 5. Fault rock permeability values from three orthogonal orientations from faults cutting similar recrystallized carbonates (juxtaposition of similar lithofacies, top), deformation bands (self-juxtaposition, middle), and those cutting different lithofaices (juxtaposition of different lithofacies, bottom). Left: Relative permeability of samples. A permeability anisotropy is observed in the majority of samples, with self- or similar juxtapositions showing the lowest permeability in the z-orientation. Right: Permeability anisotropy data. Lowest permeability is generally perpendicular to fault strike (z-orientation), for self- and similar juxtaposition. No systematic permeability anisotropy is observed in faults that juxtapose different lithofacies.

between the x- and y-oriented plugs (along-strike and down-dip slip surface, respectively) (Figure 5 left). Hence, there is no defined orientation that may create the highest permeable pathways.

Among the 60 core plugs measuring 20 samples within this category, z-plane oriented core plugs recorded the lowest permeability in 75% of the samples. Both *y*- and *x*- oriented core plugs each show a 12.5% likelihood of recording the lowest permeability. Notably, when *x*- or *y*-plane oriented core plugs exhibit the lowest permeability, the z-plane permeability is often within the same order of magnitude (e.g., Si053, Punta Negra 2, Figure 5 right). Only one sample displays a permeability more than one order of magnitude higher in the *z*-orientation (Si019a, Faro Fault, Figure 5 right). These findings suggest a greater probability of restricted across-fault fluid flow, while along or up-/down-fault fluid flow may be relatively enhanced.

In cases where the *z*-plane core plugs have the lowest recorded permeability, the value can be over five orders of magnitude lower than those of *x* or *y*-oriented core plugs (e.g., Si037, Torre Isolidda, Figure 5 right). However, there are instances where z-plane core plugs exhibit permeability within the same order of magnitude as either x- or y-oriented core plugs (e.g., Si069, Punta Negra 3, Figure 5 right). On average, z-plane core plugs have a permeability that is two orders of magnitude lower than both x- and y-plane oriented core plugs.

4.2.1.2. Deformation Bands

In all carbonate deformation band samples, the z-plane oriented core plugs show the lowest permeability (Figure 5 left). Permeability in the z-orientation ranges from one order of magnitude lower (Si050) to over four orders lower (Si055) compared to the x- or y-oriented core plugs (Figure 5 right). Three out of four samples display the highest permeability in the x-plane (Si050, Si052 and Si055, Figure 5 right). These samples are from deformation bands showing strike-slip kinematics. One sample shows the y-orientation to have a slightly higher permeability (Si049, Figure 5 right). This sample is from a deformation band showing oblique slip kinematics.

4.2.2. Juxtaposition of Different Lithofacies

In cases where different lithofacies are juxtaposed, some fault rock samples exhibit a strong permeability anisotropy (Figure 5). However, no systematic trend in the permeability anisotropy can be observed. This is evident in the relative permeability data, which shows significant scatter (Figure 5 left). The lowest permeability is recorded in the x-orientation 3 out of 19 samples, the y-orientation in nine out of 19 samples, and the z-orientation seven out of 19 times. Similarly, the highest permeability occurs in the x-orientation in 8 samples, the y-orientation in 4 samples, and the z-orientation in 7 samples.

The heterogeneity of the permeability anisotropy is further emphasized by examining variations within a single sample that has allowed for multiple orthogonal core plugs, specifically sample ma038, Qala Point Fault Zone (Figure 5 right). This sample consists of three sub-samples - ma038a, ma038b, and ma038c - each exhibiting a permeability anisotropy. However, the orientation for the lowest and highest permeability varies between sub-samples. This variability likely reflects the heterogeneity created by the variety of deformation and/or diagenetic processes active when multiple lithofacies are faulted.

Since no systematic permeability anisotropy is observed when different lithofacies are juxtaposed, our focus will primarily be on identifying and understanding the factors driving the systematic permeability anisotropy in cases where self and similar lithofacies are juxtaposed.

4.3. Microstructures

4.3.1. Juxtaposition of Self/Similar Lithofacies

4.3.1.1. Recrystallized Carbonates

Faulting within recrystallized carbonates shows extensive brecciation and cataclasis, on varying scales and intensities, with some remnant fossil clasts being observed (Figures 6a and 6c). Brecciation can range from early stage crackle breccia to complex chaotic breccias, where multi-phase and multi-scale brecciation is observed. Fault rock matrix is often observed as an interlocking crystalline texture. Where larger crystals are observed, these fault rocks also show twinning, predominantly as Type I or Type II, but occasionally show Type III twins, indicating higher temperature conditions (Burkhard, 1993; Ferrill et al., 2004) (Figures 6a and 6b). Conversely, the fault rocks can also often have a very fine-grained matrix; where significant comminution has occurred to reduce crystal size, or from the lack of recrystallization, or a combination. These fault rocks also show a high density of fractures that are partially opened, or veined (Figure 6a). In areas where there are wide shear zones, the matrix is observed to be a dark, fine-grained cataclastic texture, occasionally showing a foliation. Although some fault rocks are calcite in composition, others show dolomite replacement within the fracture matrix between the calcite clasts (Figure 6c; Kaminskaite et al., 2020).

To assess shear orientations in relation to a permeability anisotropy, we show results from sample Si088 from Punta Negra 2, where the highest permeability is in the x-orientation, while the z-orientation exhibits permeability that is three orders of magnitude lower (Figure 5 right). In this sample, the x-orientation thin section shows one dominant shear orientation, approximately 160–170° from the x-axis (Figure 7). This represents a wide Y shear. Additionally, minor shears at varying orientations are observed that create multiple intersections. Specifically, P- X- R- and R' shears are observed (Figure 7x).

10.1029/2024JB028763

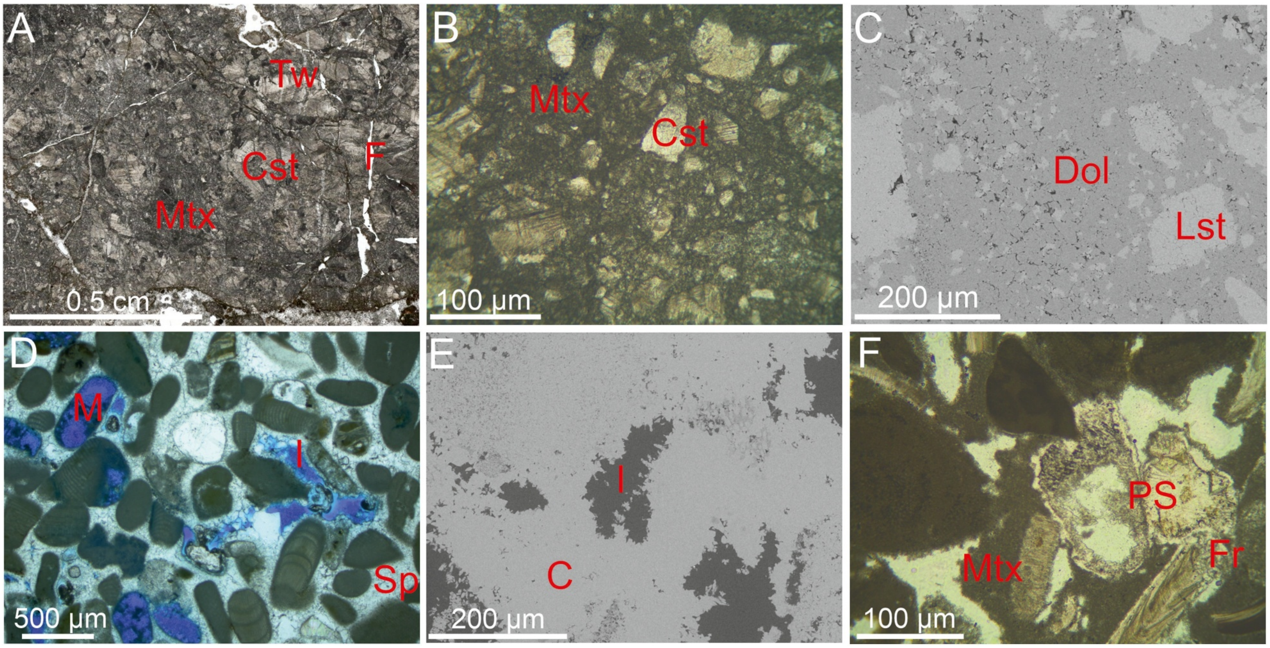

Figure 6. Optical photomicrographs (a, b, d and f) and scanning electron microscope-backscatter electron microscopy images (c) and (e) showing microstructures from fault rocks where similar recrystallized low porosity packstones have been juxtaposed (a, b and c), and deformation bands ((d and e): Castelluzo, (f): Favignana). (a) Zone of coarse breccia clasts (Cst) with crystals showing twins (Tw) and a fine-grained cataclastic matrix (Mtx) with angular breccia clasts, cut by open fractures (F), (b) Sub-angular to sub-rounded breccia clasts of varying sizes within a fine-grained cataclastic matrix, (c) Calcitic breccia clasts (Lst) surrounded by dolomitic (Dol) matrix showing some enhanced porosity due to dolomitization, (d) Intact fossils with some dissolved fossil clasts creating moldic porosity (M) with micritic rims, and drusy spar cement infilling intergranular pore space (I). Spary cement (Sp) observed surrounding intact fossils, (e) Cemented texture (C) with drusy spar infilling intergranular pore space, and (f) Fragmented fossils (Fr) showing pressure solution, with micritic matrix infilling pores.

In the *y*-oriented thin section, a broader range of shear orientations is present, but two primary shear orientations are identified: one at 40° and another between 110 and 150° from the *x*-axis (Figure 7y). These correspond to *R*- and *R*' shears, forming a conjugate system.

The z-oriented thin section, aligned along the fault strike, displays numerous shear orientations. However, two dominant shear orientations identified at 70 and 120° from the *x*-axis (Figure 7z).

4.3.1.2. Deformation Bands

As recorded in Kaminskaite et al. (2019), there are differing microstructures observed within the deformation bands at Favignana compared to those on Castelluzzo, mainland Sicily. Specifically, deformation bands at Castelluzzo show coarse grained, blocky cement within the matrix. No peloids are recorded within the bands, with moldic pores occurring instead, indicating dissolution of peloids after cementation. Pore filling cementation is evident by crystal sizes increasing away from grain boundaries, and triple junction of crystals being common (Figure 6d). Some drusy mosaic cements are observed to infill interparticle pores and molds (Figures 6d and 6e). All fossils remain intact, with no pressure solution observed, and limited compaction (Figure 6d). Conversely, deformation bands at Favignana show fragmentation of fossil clasts, disintegration of peloids, creating a widespread micritic matrix that have been neomorphosed in places. Pressure solution is also common between fossil clasts (Figure 6f).

Petrographic analysis reveals a strong alignment of both grains and pores within the deformation bands on Favignana (Figure 8, sample Si049). Sample Si049 shows the highest permeability in the y-orientation (Figure 5 right) and lowest in the *z*-orientation. The deformation band in this case formed from oblique kinematics. Examination of the three orthogonal thin sections shows a pronounced preferred alignment of grains and pores in the *x*- and *z*-oriented thin sections, which are vertically across and along the fault, respectively. However, no preferred alignment is observed in the y-oriented thin section, which is horizontal along the fault (Figure 8).

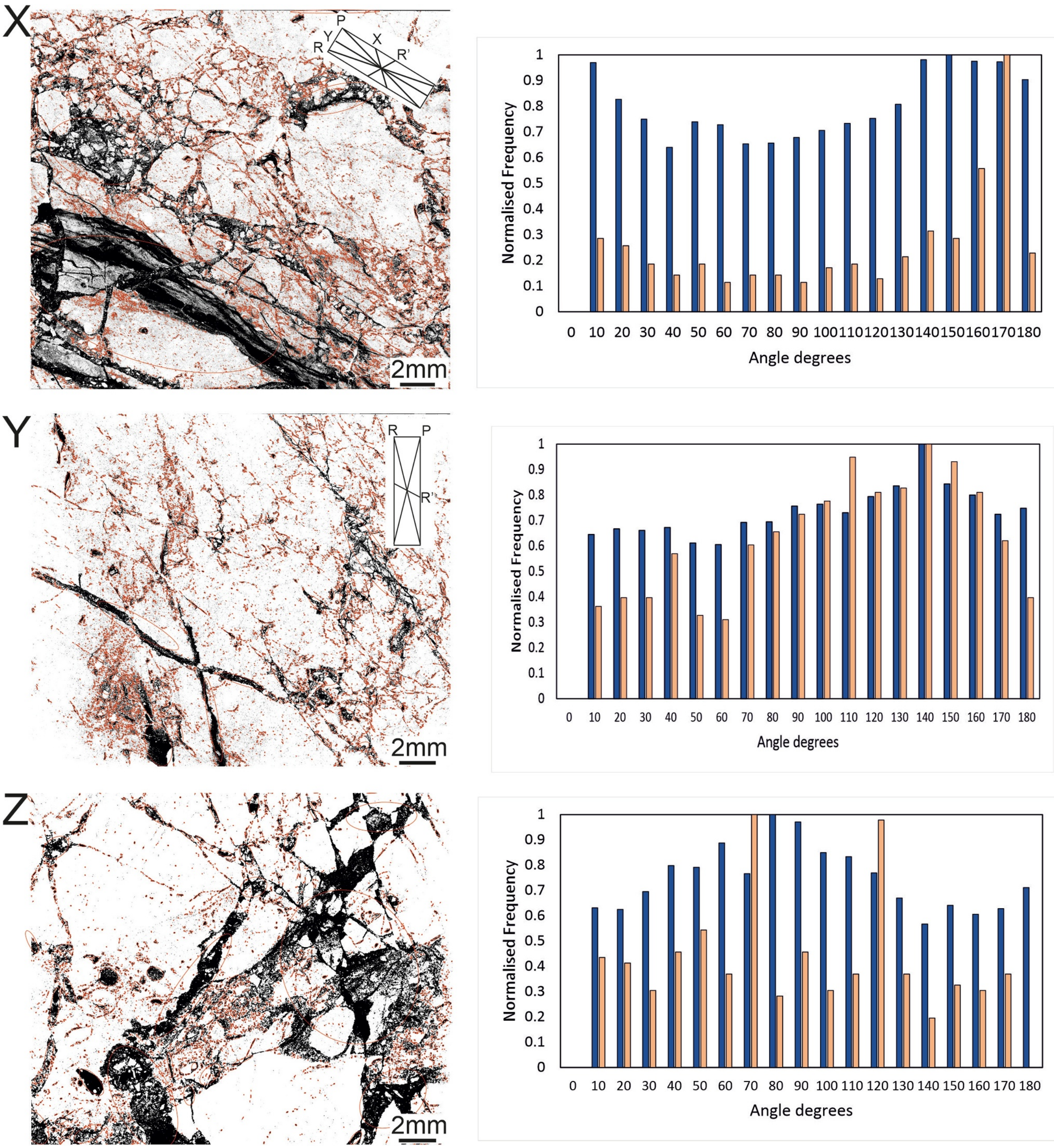

Figure 7. Image analysis of full thin section images from recrystallized fault rock sample Si088, in x- y- and z- orientations (see Michie et al., 2024 for data). Left: threshold images showing all best-fit ellipses used for analysis. Right: Results of shear orientations, where Angle is the angle between primary axis of the ellipse and a line parallel to the *x*-axis of the image. Blue: normalized data from all shears over 0.001 mm^2. Orange: normalized area-weighted from shears larger than 0.01 mm^2. In this sample (Si088), *x*-oriented core plugs show the highest permeability, and *z*-oriented core plugs show the lowest permeability (see Figure 5).

Although 2D thin sections allow for a quick assessment of grain and pore orientation, they do not capture the overall 3D shape and orientation of the pores. To address this, we utilized micro-CT scans to visualize and quantify pore orientation in 3D space. The angles measured represent rotation about different planes: Phi (XY plane), Theta (XZ plane) and Psi (XY plane) (Figure 9, sample Si049). Each core plug exhibits a preferred

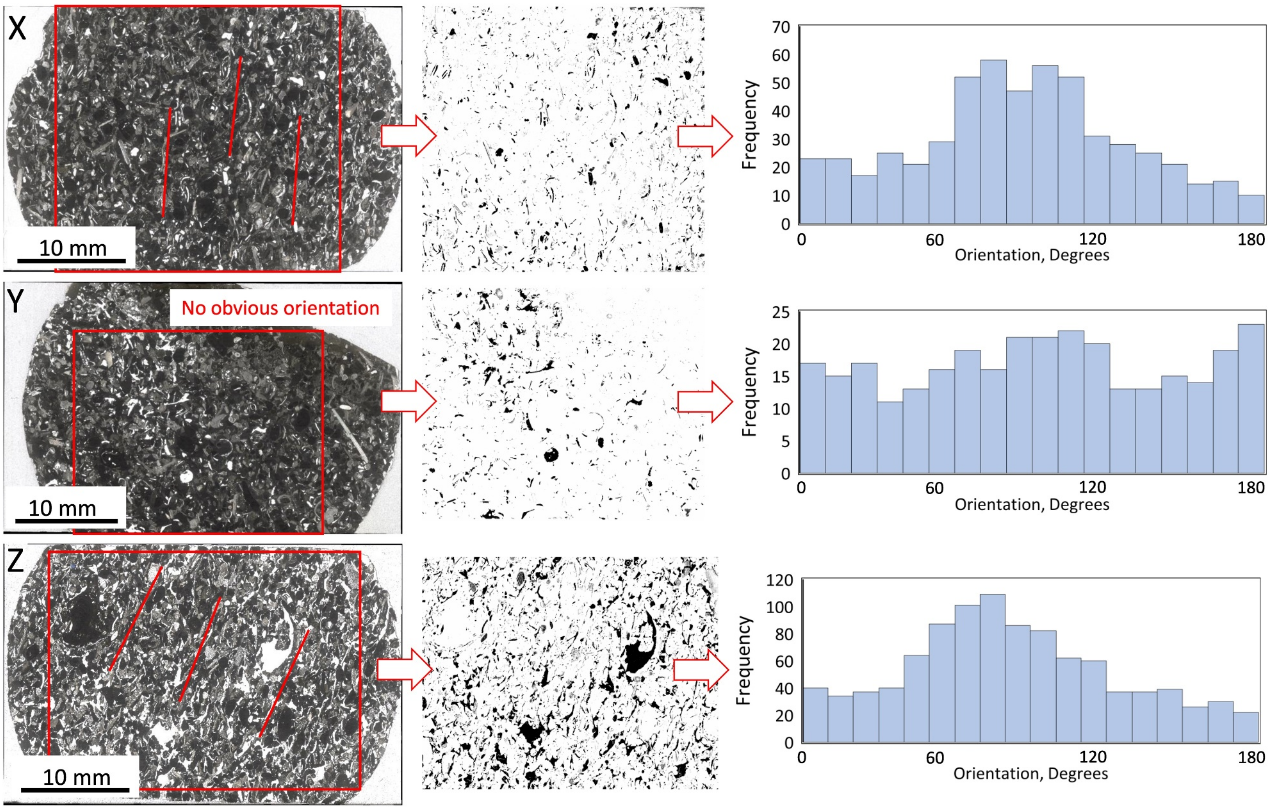

Figure 8. Image analysis of full thin sections in the *x*- *y*- and *z*- orientation from si049. Left: Thin section images indicating grain and pore elongation trends (red lines). Red boxes indicate size and location of the cropped image used for image analysis. Center: Isolated pores after thesholding. Right: Resulting ellipse angle of the pores. A clear orientation is observed for the *x*- and *z*- oriented thin sections, whilst no obvious orientation is observed or recorded for the y-oriented thin section.

orientation in two out of the three planes: the x-oriented core plug in the XY and XZ planes, the *y*-oriented core plug in the XZ and YZ planes, and the z-oriented core plug in the XY and XZ planes (Figure 9). Hence, the pores are aligned at a slightly oblique angle down the deformation band, that is, in the *y*-orientation.

4.3.2. Juxtaposition of Different Lithofacies

At juxtapositions of different lithofacies, the microstructures are observed to vary with the differing lithofacies, such that a variety of deformation and diagenetic microstructures are observed along fault-strike.

The South Qala Fault juxtaposes the BC Formation next to the LGL Formation, that is, a marl next to wackestone. The microstructures vary from cementation, through-going fracturing and brecciation within finer-grained layers, to cataclasis (i.e., clast-confined fracturing and comminution) observed within coarser layers that contain more benthic foraminifera and bivalves (Figures 9a and 9b; Cooke et al., 2018). Some larger intact fossils remain.

The Victoria Lines Fault juxtaposes the LGL Formation next to the Xlendi Mb of the LCL Formation, that is, a wackestone next to a bioclastic packstone (Michie, Kaminskaite, et al., 2021). Along the principal slip surface, the microstructures can vary from breccias or cataclasites (Figures 10c and e), to purely diagenetic processes creating cemented fault rocks (Figure 10d), over a small distance. A variety of overprinting textures are also observed, creating patches of dissolution and/or fracturing (Figure 10d).

The Qala Point Fault Zone juxtaposes the Xlendi Mb of the LCL Formation against the Attard Mb of the LCL Formation, that is, a bioclastic packstone against an algal-rich packstone (Cooke et al., 2018). The bioclastic packstone generally exhibits cataclastic textures, showing fragmented fossil clasts within a fine-grained matrix that shows some cementation (Figure 10f). Conversely, the algal-rich packstone deforms by brecciation, where the breccia clasts vary in size and often be classed as mosaic breccia. The breccia clasts can either be intact or

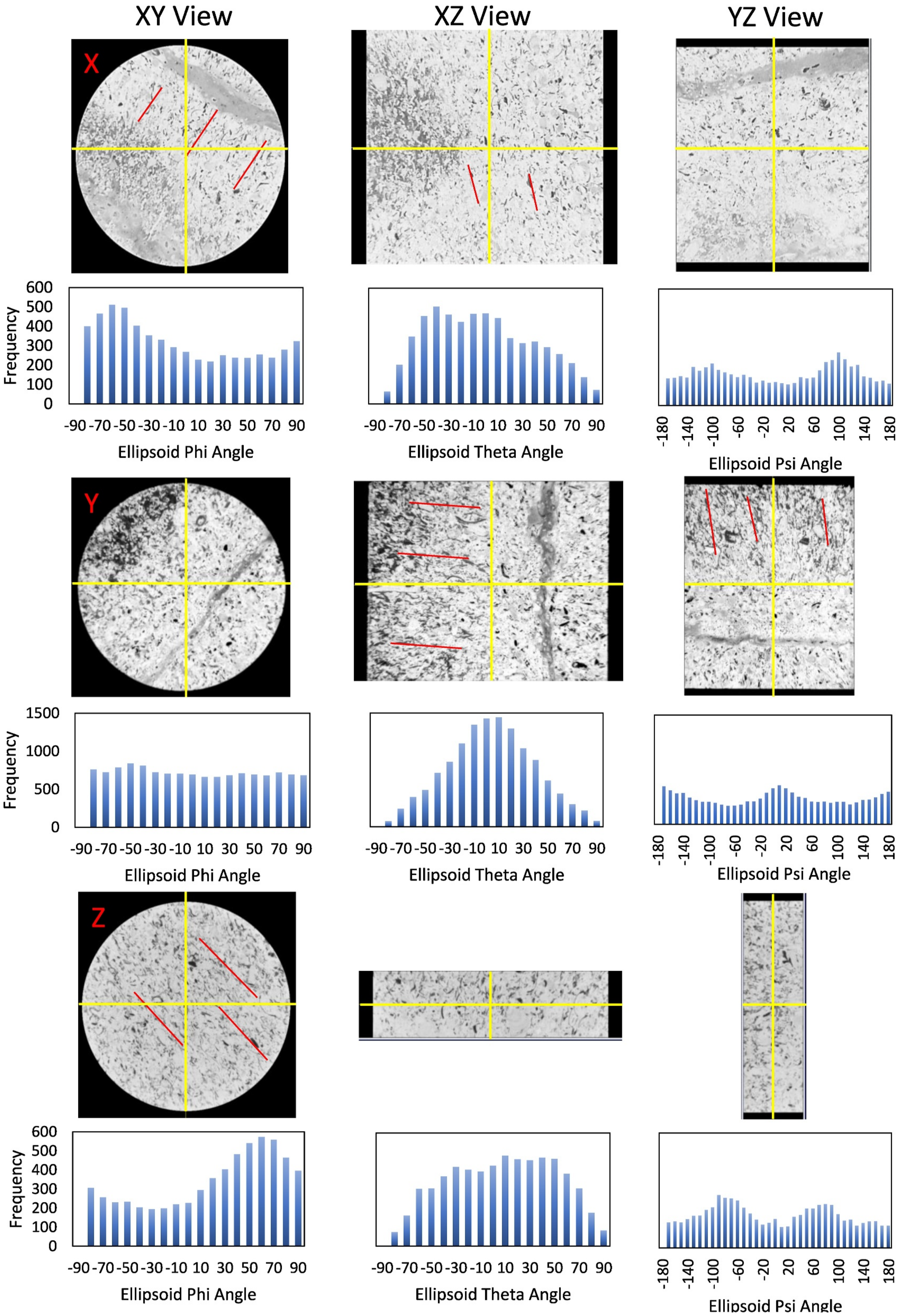

Figure 9. Micro-CT images and measurement results for core plugs taken in the *x*- *y*- and *z*-orientation from sample Si049. Images are shown in the XY (horizontal slices through the core plug), XZ and XY (orthogonal vertical slices down the core plugs) views. Histograms below the micro-CT images show results from the three angles from the best fit ellipsoid shapes: rotation about the XY (Phi Angle), XZ (Theta Angle) and XY (Psi Angle) planes.

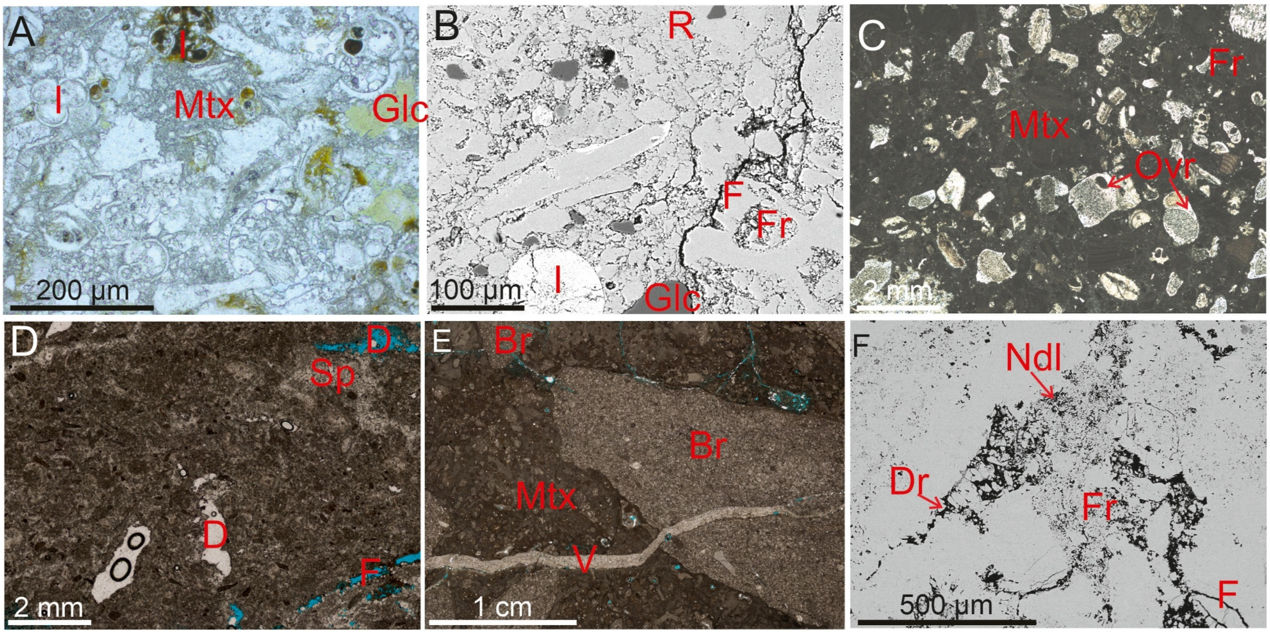

Figure 10. Optical photomicrographs (a, c, d and f) and scanning electron microscope-backscatter electron microscopy images (b) and (f) showing microstructures from fault rock where juxtaposition of different lithofacies has occurred on Malta ((a and b): South Qala Fault (c, d, e): Victoria Lines Fault, (f): Qala Fault). (a) Intact larger fossil clasts (I) surrounded by fine-grained fragmented matrix (Mtx). Some glauconite clasts observed (Glc), (b) Occasional intact clasts, but with the majority of the clasts being fragmented (Fr) and recyrstallised (R). Cut by an open fracture (F), (c) Cataclastic texture with sub-rounded fragmented clasts commonly showing overgrowth cements (Ovr) within a fine-grained catalcastic matrix, (d) Zones of aggrading neomorphism create a patchy coarse-grained spar (Sp), surrounded by finer micritic matrix. Areas of dissolution (D) and fracturing apparent, (e) Large recrystallized breccia clasts (Br) surrounded by a fine-grained matrix (Mtx), cross-cut by a large vein (V), (f) Drusy mosaic (Dr) cements infilling intergranular pores, as well as more needle-like crystals (Ndl). Fragmented texture observed, cut by some open fractures.

recrystallized. The overall brecciation texture often shows signs of rhizogenic microstructures, indicating exploitation of a higher permeability conduit by vegetation.

5. Discussion

5.1. Causes of Permeability Anisotropy

5.1.1. Recrystallized Carbonates

Although all documented microstructures will influence the permeability, it is unlikely that they all will contribute to the permeability anisotropy, due to lack of oriented fabrics, such as breccias. Further, the low porosity means pore orientation is unlikely to be a major contributor to the permeability anisotropy measured (similar to that described by Farrell et al., 2014). However, preferentially aligned fractures, veins or shears, specifically wide *R*- and *Y*- shears are likely to create the permeability anisotropy (similar to that described by Faulkner & Rutter, 1998).

As shown in Si088 (Figure 7), where the highest permeability is in the *x*-orientation, and lowest in the *z*-orientation, the wide *Y*-shears observed in the *x*-oriented core plugs will likely facilitate flow along the fault while restricting flow (lowering permeability) across it. The wide range of shear orientations observed in the *y*- and *z*-oriented thin sections, create numerous intersections that are likely to facilitate increased flow along the fault. This result aligns with previous studies on foliated fault rock (e.g., Evans et al., 1997; Faulkner & Rutter, 1998; Sibson, 2000; Wibberley and Shimamoto, 2005), where stress-controlled microstructures - such as foliations, fractures, veins or Reidel shears–contribute to the lowest permeability perpendicular to foliation or slip surface. However, prior research suggests that intersections of these microstructures parallel to σ_2 can create a maximum permeability in this direction (e.g., Cavailhes et al., 2013; Faulkner & Rutter, 1998; Wibberley and Shimamoto, 2005), a pattern not consistently shown in our results. This discrepancy may be due to an extensional tectonic phase being overprinted by later strike-slip faulting, where the creation of newly oriented shears during a reactivation period may have altered the expected direction of maximum permeability. Hence, tectonic history may prove crucial in predicing a permeability anisotropy.

5.1.2. Deformation Bands

Permeability anisotropy in deformation bands cutting high porosity carbonates appears to be created from pore alignment. As shown in Figure 9, the strongest preferred pore orientation in sample Si049 is observed within the *y*-oriented core plug in the XZ plane, where the pores are aligned at a slightly oblique angle down the core plug. This explains the absence of a preferred alignment in the *y*-oriented thin section (Figure 8). Hence, alignment of the grains and pores appear to be oriented fault parallel, down fault-dip, resulting in the highest permeability at a low angle to σ_1, that is, in the direction of transport. This finding is consistent with previous studies despite differences in lithological composition (e.g., Farrell et al., 2014; Zhu et al., 2002). However, in contract to Farrell et al. (2014), the minimum permeability is oriented at a low angle to σ_3, thereby creating reduced flow perpendicular to the fault/band surface.

Although pore orientation play a key role in the creation of a permeability anisotropy, the development of clustered deformation bands may also contribute. Thes clustered bands consist of multiple bands in close proximity, each reducing permeability and restricting flow across the cluster. Consequently, core plugs in the *z*-orientation, which intersect more bands perpendicular to the core plug, exhibit the lowest permeability.

5.1.3. Different Lithofacies

Since host material is considered isotropic, the permeability anisotropy observed within the fault rocks is likely a result of the deformation and/or diagenetic mechanisms active during faulting. However, the lack of a consistent permeability anisotropy likely reflects the significant heterogeneity in fault rock types along fault-strike, where significant variations in deformation and diagenetic microstructures are observed over short distances. Consequently, any microstructures that might otherwise generate a systematic permeability anisotropy are obscured by the diverse range of fault textures.

5.2. Permeability Ellipsoids

A permeability anisotropy is observed in all fault rock samples analyzed for this contribution. However, the nature and cause of the permeability anisotropy varies with lithofacies and juxtaposition.

Deformation band development typically involves grain breakdown and grain/pore reorganization, which leads to pores alignment at a low angle to σ_1, resulting in a maximum permeability along band-strike and the minimum permeability oriented at a low angle to σ_3, reducing flow perpendicular to band (Figure 11 left).

Juxtaposition of similar recrystallized, low porosity carbonates results in the lowest permeability being oriented perpendicular to fault strike, associated with Reidel shear development. However, the maximum permeability varies between along-strike and down fault-dip orientations, that is, at a low angle to σ_1 or parallel to σ_2, respectively (Figure 11 middle), associated with multiple reactivation episodes, generating new shear intersections.

The magnitude of permeability anisotropy has been recorded to vary across studies, ranging from 1 to 1.5 orders of magnitude in experimental methods (Zhang et al., 1999; Zhang & Tullis, 1998), three orders of magnitude in clay-bearing fault gouge outcrops (Faulkner & Rutter, 1998) and granite (Evans et al., 1997), to up to five orders of magnitude in a high porosity sandstone fault (Farrell et al., 2014). This study shows a permeability anisotropy exceeding five orders of magnitude in some samples, with an average of around two orders of magnitude, which is comparable to previous findings, despite the differences in lithologies.

The wide range of deformation and diagenetic mechanisms active during the juxtaposition of different lithofacies prevents the formation of a systematic permeability anisotropy, instead introducing heterogeneity along fault-strike (Figure 11 right). Additionally, the mechanisms do not create significant shears or an aligned pore network. This raises an important question: is the lack of systematic permeability anisotropy in these scenarios a product of heterogeneity, or do these lithotypes simply not deform in a way that could generate an anisotropy? A change in tectonic conditions, displacement and burial depth may alter stress conditions and hence deformation style, potentially fostering mechanisms favorable to permeability anisotropy development.

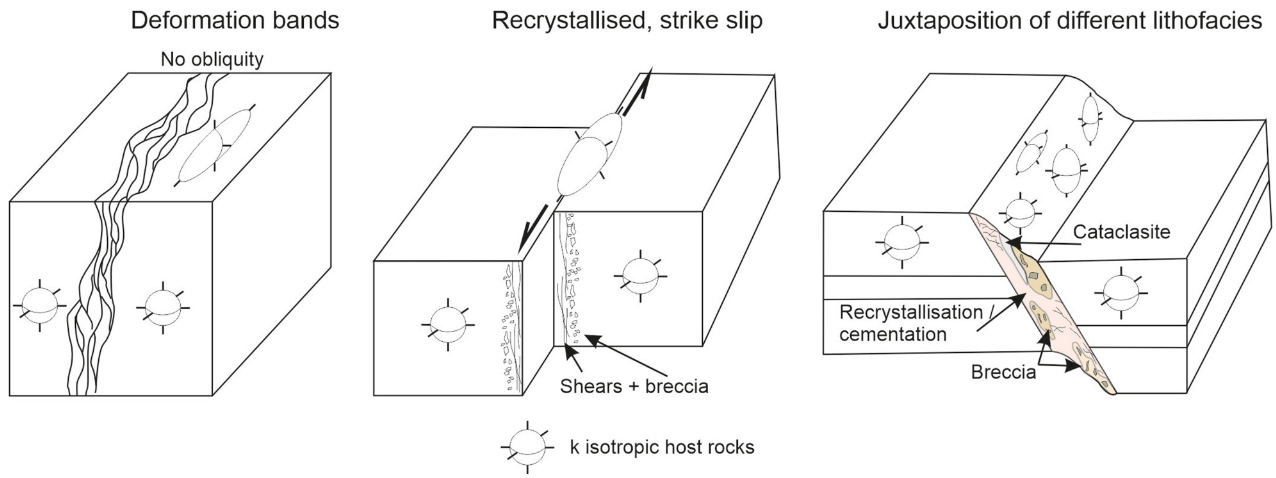

Figure 11. Schematic models illustrating the permeability ellipsoid for each scenario: deformation bands (self-juxtaposition; left), similar juxtaposition in low porosity, recrystallized carbonates that have experienced strike slip kinematics (middle), and juxtaposition of different lithofacies (right).

6. Summary

- An isotropic permeability is recorded in all studied host rock samples.
- A permeability anisotropy is recorded in all carbonate fault rock samples.
- A systematic permeability anisotropy in carbonate fault rocks is only observed where self- or similar juxtaposition occurs such as deformation bands in high porosity grainstones or faulting in recrystallized carbonates. However, when different lithofacies are juxtaposed, no systematic permeability anisotropy is observed.
- At self- or similar juxtaposition, the lowest permeability is recorded across the fault, parallel or sub-parallel to σ_3, where the permeability can be up to five orders of magnitude lower than along- or normal to fault slip.
- Faulting in recrystallized carbonates is influenced by intersecting shears and fractures. The lowest permeability occurs perpendicular to fault strike, associated with the development of wide *Y*-shears. The highest permeability occurs both along- and normal to fault slip, parallel to σ_2 or at a low angle to σ_1, with shear connectivity appearing to be similar in both orientations, reflecting a complex tectonic history and multiple reactivation episodes.
- Deformation bands in carbonates show the lowest permeability sub-parallel to σ_3, with the maximum permeability at a low angle to σ_1 created by pore alignment in the direction of transport.
- When juxtaposition of different lithofacies occurs, the highest and lowest permeability can occur in any orientation. A variety of deformation and/or diagenetic mechanisms can be active in these scenarios, creating significant heterogeneity in the resulting microstructures along fault-strike, obscuring any systematic permeability anisotropy that may be formed.

Data Availability Statement

Supporting information includes example of raw permeability measurements in Supporting Information S1. The permeability and image analysis data used within this paper are available at (Michie et al., 2024), under license Create Commons: Attribution 4.0.

Acknowledgments
Many thanks are given to ADNOC, ENI, OMV, Petrobras and Wintershall DEA for sponsoring the Carbonate Fault Rock project, allowing the collection of data for this analysis. A huge thank you goes to Julia Behnsen, the laboratory technician for the micro-CT for the processing of the data and for guidance on the analysis. A further thanks goes to Josh Hicks for help with full section scans of the thin sections. Many thanks go to Thibault Cavailhes, five anonymous reviewers and editor Yves Bernabe for their thorough and constructive feedback that has significantly improved the quality of this paper.

References

Abate, B. (1993). Università di Palermo. Dipartimento di geologia e geodesia. Carta geologica dei monti di Capo San Vito.

Abate, B., Incandela, A., & Renda, P. (1997). Dipartimento di Geologia e Geodesia, Universiy. Carta Geologica delle Isole di Favignana e Levanzo.

Agosta, F., Alessandroni, M., Antonellini, M., Tondi, E., & Giorgioni, M. (2010). From fractures to flow: A field-based quantitative analysis of an outcropping carbonate reservoir. *Tectonophysics*, *490*(3–4), 197–213. https://doi.org/10.1016/j.tecto.2010.05.005

American Petroleum Institute. (1998). *Recommended practice 40: Recommended practices for core analysis* (2nd ed.). American Petroleum Institute.

Antonellini, M., & Aydin, A. (1994). Effect of faulting on fluid flow in porous sandstones: Petrophysical properties. *AAPG Bulletin*, *78*(3), 355–377. https://doi.org/10.1306/bdff90aa-1718-11d7-8645000102c1865d

Arch, J., & Maltman, A. (1990). Anisotropic permeability and tortuosity in deformed wet sediments. *Journal of Geophysical Research*, *95*(B6), 9035–9045. https://doi.org/10.1029/jb095ib06p09035

Aydin, A. (2000). Fractures, faults, and hydrocarbon entrapment, migration and flow. *Marine and Petroleum Geology*, *17*(7), 797–814. https://doi.org/10.1016/s0264-8172(00)00020-9

Ballas, G., Fossen, H., & Soliva, R. (2015). Factors controlling permeability of cataclastic deformation bands and faults in porous sandstone reservoirs. *Journal of Structural Geology*, *76*, 1–21. https://doi.org/10.1016/j.jsg.2015.03.013

Bense, V. F., & Person, M. A. (2006). Faults as conduit-barrier systems to fluid flow in siliciclastic sedimentary aquifers. *Water Resources Research*, *42*(5). https://doi.org/10.1029/2005wr004480

Bjørnarå, T. I., Skurtveit, E., Michie, E. A., & Smith, S. A. (2023). Characterising along-and across-fault fluid flow properties for assessing flow rates and overburden fluid migration along faults-A case study from the North Sea. *Petroleum Geoscience*, *29*(3). petgeo2023-033. https://doi.org/10.1144/petgeo2023-033

Bonson, C. G., Childs, C., Walsh, J. J., Schöpfer, M. P., & Carboni, V. (2007). Geometric and kinematic controls on the internal structure of a large normal fault in massive limestones: The Maghlaq fault, Malta. *Journal of Structural Geology*, *29*(2), 336–354. https://doi.org/10.1016/j.jsg.2006.06.016

Burkhard, M. (1993). Calcite twins, their geometry, appearance and significance as stress-strain markers and indicators of tectonic regime: A review. *Journal of Structural Geology*, *15*(3–5), 351–368. https://doi.org/10.1016/0191-8141(93)90132-t

Caine, J. S., Evans, J. P., & Forster, C. B. (1996). Fault zone architecture and permeability structure. *Geology*, *24*(11), 1025–1028. https://doi.org/10.1130/0091-7613(1996)024<1025:fzaaps>2.3.co;2

Catalano, R., D'argenio, B., Montanari, L., Morlotti, E., & Torelli, L. (1985). Marine geology of the NW Sicily offshore (Sardinia Channel) and its relationships with mainland structures. *Bollettino della Societa Geologica Italiana*, *104*(2), 207–215.

Cavailhes, T., Sizun, J. P., Labaume, P., Chauvet, A., Buatier, M., Soliva, R., et al. (2013). Influence of fault rock foliation on fault zone permeability: The case of deeply buried arkosic sandstones (Gres d'Annot, southeastern France). *AAPG Bulletin*, *97*(9), 1521–1543. https://doi.org/10.1306/03071312127

Chester, F. M., & Logan, J. M. (1986). Implications for mechanical properties of brittle faults from observations of the Punchbowl fault zone, California. *Pure and Applied Geophysics*, *124*(1–2), 79–106. https://doi.org/10.1007/bf00875720

Continental Shelf Department Malta. (2022). Geological map of the Maltese Islands. Accessible online at: Retrieved from https://continentalshelf.gov.mt/download-geological-map-data/

Cooke, A. P., Fisher, Q. J., Michie, E. A., & Yielding, G. (2018). Investigating the controls on fault rock distribution in normal faulted shallow burial limestones, Malta, and the implications for fluid flow. *Journal of Structural Geology*, *114*, 22–42. https://doi.org/10.1016/j.jsg.2018.05.024

Crawford, B. R. (1998). Experimental fault sealing: Shear band permeability dependency on cataclastic fault gouge characteristics. *Geological Society, London, Special Publications*, *127*(1), 27–47. https://doi.org/10.1144/gsl.sp.1998.127.01.04

Cuisiat, F., & Skurtveit, E. (2010). An experimental investigation of the development and permeability of clay smears along faults in uncemented sediments. *Journal of Structural Geology*, *32*(11), 1850–1863. https://doi.org/10.1016/j.jsg.2009.12.005

Dart, C. J., Bosence, D. W. J., & McClay, K. R. (1993). Stratigraphy and structure of the Maltese graben system. *Journal of the Geological Society*, *150*(6), 1153–1166. https://doi.org/10.1144/gsjgs.150.6.1153

Evans, J. P., Forster, C. B., & Goddard, J. V. (1997). Permeability of fault-related rocks, and implications for hydraulic structure of fault zones. *Journal of Structural Geology*, *19*(11), 1393–1404. https://doi.org/10.1016/s0191-8141(97)00057-6

Farrell, N. J. C., Healy, D., & Taylor, C. W. (2014). Anisotropy of permeability in faulted porous sandstones. *Journal of Structural Geology*, *63*, 50–67. https://doi.org/10.1016/j.jsg.2014.02.008

Faulkner, D. R., Jackson, C. A. L., Lunn, R. J., Schlische, R. W., Shipton, Z. K., Wibberley, C. A. J., & Withjack, M. O. (2010). A review of recent developments concerning the structure, mechanics and fluid flow properties of fault zones. *Journal of Structural Geology*, *32*(11), 1557–1575. https://doi.org/10.1016/j.jsg.2010.06.009

Faulkner, D. R., & Rutter, E. H. (1998). The gas permeability of clay-bearing fault gouge at 20 C. *Geological Society, London, Special Publications*, *147*(1), 147–156. https://doi.org/10.1144/gsl.sp.1998.147.01.10

Ferraro, F., Agosta, F., Prasad, M., Vinciguerra, S., Violay, M., & Giorgioni, M. (2020). Pore space properties in carbonate fault rocks of peninsular Italy. *Journal of Structural Geology*, *130*, 103913. https://doi.org/10.1016/j.jsg.2019.103913

Ferrill, D. A., & Morris, A. P. (2003). Dilational normal faults. *Journal of Structural Geology*, *25*(2), 183–196. https://doi.org/10.1016/s0191-8141(02)00029-9

Ferrill, D. A., Morris, A. P., Evans, M. A., Burkhard, M., Groshong, R. H., & Onasch, C. M. (2004). Calcite twin morphology: A low-temperature deformation geothermometer. *Journal of Structural Geology*, *26*(8), 1521–1529. https://doi.org/10.1016/j.jsg.2003.11.028

Fisher, Q. J., & Knipe, R. (1998). Fault sealing processes in siliciclastic sediments. *Geological Society, London, Special Publications*, *147*(1), 117–134. https://doi.org/10.1144/gsl.sp.1998.147.01.08

Flodin, E. A., Aydin, A., Durlofsky, L. J., & Yeten, B. (2001). Representation of fault zone permeability in reservoir flow models. SPE. In *SPE annual technical conference and exhibition?* SPE.71617.

Flodin, E. A., Gerdes, M., Aydin, A., Wiggins, W. D., Sorkhabi, R., & Tsuji, Y. (2005). Petrophysical properties of cataclastic fault rock in sandstone. *Jab*, *1*(2), 3.

Fossen, H., Schultz, R. A., Shipton, Z. K., & Mair, K. (2007). Deformation bands in sandstone: A review. *Journal of the Geological Society*, *164*(4), 755–769. https://doi.org/10.1144/0016-76492006-036

Giunta, G., Nigro, F., & Renda, P. (2000). Extensional tectonics during Maghrebides chain building since late Miocene: Examples from northern Sicily. *Annales Societatis Geologorum Poloniae*, *70*(1), 81–98.

Grove, C., & Jerram, D. A. (2011). jPOR: An ImageJ macro to quantify total optical porosity from blue-stained thin sections. *Computers and Geosciences*, *37*(11), 1850–1859. https://doi.org/10.1016/j.cageo.2011.03.002

Healy, D. (2009). Anisotropy, pore fluid pressure and low angle normal faults. *Journal of Structural Geology*, *31*(6), 561–574. https://doi.org/10.1016/j.jsg.2009.03.001

Healy, D. (2012). Anisotropic poroelasticity and the response of faulted rock to changes in pore-fluid pressure. *Geological Society, London, Special Publications*, *367*(1), 201–214. https://doi.org/10.1144/sp367.14

Jones, S. C. (1997). A technique for faster pulse-decay permeability measurements in tight rocks. *SPE Formation Evaluation*, *12*(1), 19–25.

Kaminskaite, I., Fisher, Q. J., & Michie, E. A. H. (2019). Microstructure and petrophysical properties of deformation bands in high porosity carbonates. *Journal of Structural Geology*, *119*, 61–80. https://doi.org/10.1016/j.jsg.2018.12.001

Kaminskaite, I., Fisher, Q. J., & Michie, E. A. H. (2020). Faults in tight limestones and dolostones in San Vito lo Capo, Sicily, Italy: Internal architecture and petrophysical properties. *Journal of Structural Geology*, *132*, 103970. https://doi.org/10.1016/j.jsg.2019.103970

Kettermann, M., Smeraglia, L., Morley, C. K., von Hagke, C., & Tanner, D. C. (2020). Fault sealing. In *Understanding faults* (pp. 283–350). Elsevier.

Kim, Y. S., Peacock, D. C., & Sanderson, D. J. (2004). Fault damage zones. *Journal of Structural Geology*, *26*(3), 503–517. https://doi.org/10.1016/j.jsg.2003.08.002

Kim, Y. S., Peacock, D. C. P., & Sanderson, D. J. (2003). Mesoscale strike-slip faults and damage zones at Marsalforn, Gozo Island, Malta. *Journal of Structural Geology*, *25*(5), 793–812. https://doi.org/10.1016/s0191-8141(02)00200-6

Klinkenberg, L. J. (1941). The permeability of porous media to liquids and gases. *Drilling and Production Practice*, 200–213.

Knipe, R. J., Jones, G., & Fisher, Q. J. (1998). Faulting, fault sealing and fluid flow in hydrocarbon reservoirs: An introduction. *Geological Society, London, Special Publications*, *147*(1). vii-xxi. https://doi.org/10.1144/gsl.sp.1998.147.01.01

Kopf, A. (2001). Permeability variation across an active low-angle detachment fault, western Woodlark Basin (ODP Leg 180), and its implication for fault activation. *Geological Society, London, Special Publications*, *186*(1), 23–41. https://doi.org/10.1144/gsl.sp.2001.186.01.03

Legland, D., Arganda-Carreras, I., & Andrey, P. (2016). MorphoLibJ: Integrated library and plugins for mathematical morphology with ImageJ. *Bioinformatics*, *32*(22), 3532–3534. https://doi.org/10.1093/bioinformatics/btw413

Michie, E., Kaminskaite, I., Cooke, A., & Fisher, Q. (2024). Permeability anisotropy data of Carbonate Fault Rocks [dataset]. In *AGU solid earth*. Zenodo. https://doi.org/10.5281/zenodo.12699472

Michie, E. A. H., Cooke, A. P., Kaminskaite, I., Stead, J. C., Plenderleith, G. E., Tobiss, S. D., et al. (2021). Key controls on the hydraulic properties of fault rocks in carbonates. *Petroleum Geoscience*, *27*(2). petgeo2020-034. https://doi.org/10.1144/petgeo2020-034

Michie, E. A. H., & Haines, T. J. (2016). Variability and heterogeneity of the petrophysical properties of extensional carbonate fault rocks, Malta. *Petroleum Geoscience*, *22*(2), 136–152. https://doi.org/10.1144/petgeo2015-027

Michie, E. A. H., Haines, T. J., Healy, D., Neilson, J. E., Timms, N. E., & Wibberley, C. A. J. (2014). Influence of carbonate facies on fault zone architecture. *Journal of Structural Geology*, *65*, 82–99. https://doi.org/10.1016/j.jsg.2014.04.007

Michie, E. A. H., Kaminskaite, I., Cooke, A. P., Fisher, Q. J., Yielding, G., & Tobiss, S. D. (2021). Along-strike permeability variation in carbonate-hosted fault zones. *Journal of Structural Geology*, *142*, 104236. https://doi.org/10.1016/j.jsg.2020.104236

Nabawy, B. S. (2018). Impacts of fossil anisotropy on the electric and permeability anisotropy of highly fossiliferous limestone: A case study. *Marine Geophysical Researches*, *39*(4), 537–550. https://doi.org/10.1007/s11001-017-9335-2

Pedley, H. M., House, M. R., & Waugh, B. (1976). The geology of Malta and Gozo. *Proceedings of the Geologists' Association*, *87*(3), 325–341. https://doi.org/10.1016/s0016-7878(76)80005-3

Qu, D., & Tveranger, J. (2016). Incorporation of deformation band fault damage zones in reservoir models. *AAPG Bulletin*, *100*(3), 423–443. https://doi.org/10.1306/12111514166

Rasband, W. S. (2018). *ImageJ*. U. S. National Institutes of Health. 1997-2018 Retrieved from https://imagej.nih.gov/ij/

Sahin, A., Ali, A. Z., Saner, S., & Menouar, H. (2007). Permeability anisotropy distributions in an upper Jurassic carbonate reservoir, eastern Saudi Arabia. *Journal of Petroleum Geology*, *30*(2), 147–158. https://doi.org/10.1111/j.1747-5457.2007.00147.x

Sato, M., Takemura, T., & Takahashi, M. (2018). Development of the permeability anisotropy of submarine sedimentary rocks under true triaxial stresses. *International Journal of Rock Mechanics and Mining Sciences*, *108*, 118–127. https://doi.org/10.1016/j.ijrmms.2018.06.010

Schueller, S., Braathen, A., Fossen, H., & Tveranger, J. (2013). Spatial distribution of deformation bands in damage zones of extensional faults in porous sandstones: Statistical analysis of field data. *Journal of Structural Geology*, *52*, 148–162. https://doi.org/10.1016/j.jsg.2013.03.013

Seeburger, D. A. (1981). *Studies of natural fractures, fault zone permeability, and a pore space-permeability model*. Stanford University.

Shipton, Z. K., Evans, J. P., Robeson, K. R., Forster, C. B., & Snelgrove, S. (2002). Structural heterogeneity and permeability in faulted eolian sandstone: Implications for subsurface modeling of faults. *AAPG Bulletin*, *86*(5), 863–883. https://doi.org/10.1306/61eedbc0-173e-11d7-8645000102c1865d

Sibson, R. H. (1977). Fault rocks and fault mechanisms. *Journal of the Geological Society*, *133*(3), 191–213. https://doi.org/10.1144/gsjgs.133.3.0191

Sibson, R. H. (1994). Crustal stress, faulting and fluid flow. *Geological Society, London, Special Publications*, *78*(1), 69–84. https://doi.org/10.1144/gsl.sp.1994.078.01.07

Sibson, R. H. (2000). Fluid involvement in normal faulting. *Journal of Geodynamics*, *29*(3–5), 469–499. https://doi.org/10.1016/s0264-3707(99)00042-3

Smeraglia, L., Mercuri, M., Tavani, S., Pignalosa, A., Kettermann, M., Billi, A., & Carminati, E. (2021). 3D Discrete Fracture Network (DFN) models of damage zone fluid corridors within a reservoir-scale normal fault in carbonates: Multiscale approach using field data and UAV imagery. *Marine and Petroleum Geology*, *126*, 104902. https://doi.org/10.1016/j.marpetgeo.2021.104902

Stead, J. (2018). *The impact of burial history on the permeability of carbonate-hosted faults*. MSc thesis. University of Leeds.

Sun, H., Vega, S., & Tao, G. (2017). Analysis of heterogeneity and permeability anisotropy in carbonate rock samples using digital rock physics. *Journal of Petroleum Science and Engineering*, *156*, 419–429. https://doi.org/10.1016/j.petrol.2017.06.002

Tondi, E., Cilona, A., Agosta, F., Aydin, A., Rustichelli, A., Renda, P., & Giunta, G. (2012). Growth processes, dimensional parameters and scaling relationships of two conjugate sets of compactive shear bands in porous carbonate grainstones, Favignana Island, Italy. *Journal of Structural Geology*, *37*, 53–64. https://doi.org/10.1016/j.jsg.2012.02.003

Tondi, E., Zampieri, D., Giunta, G., Renda, P., Alessandroni, M., Unti, M., et al. (2006). Active faults and inferred seismic sources in the San Vito lo Capo peninsula, northwestern Sicily, Italy. *Geological Society, London, Special Publications*, *262*(1), 365–377. https://doi.org/10.1144/gsl.sp.2006.262.01.22

Torabi, A., Balsamo, F., Nogueira, F. C., Vasconcelos, D. L., Silva, A. C., Bezerra, F. H., & Souza, J. A. (2021). Variation of thickness, internal structure and petrophysical properties in a deformation band fault zone in siliciclastic rocks. *Marine and Petroleum Geology*, *133*, 105297. https://doi.org/10.1016/j.marpetgeo.2021.105297

Torabi, A., Fossen, H., & Alaei, B. (2008). Application of spatial correlation functions in permeability estimation of deformation bands in porous rocks. *Journal of Geophysical Research*, *113*(B8). https://doi.org/10.1029/2007jb005455

Vrolijk, P. J., Urai, J. L., & Kettermann, M. (2016). Clay smear: Review of mechanisms and applications. *Journal of Structural Geology*, *86*, 95–152. https://doi.org/10.1016/j.jsg.2015.09.006

Wibberley, C. A., & Shimamoto, T. (2005). Earthquake slip weakening and asperities explained by thermal pressurization. *Nature*, *436*(7051), 689–692. https://doi.org/10.1038/nature03901

Widarsono, B., Muladi, A., & Jaya, I. (2006). Permeability vertical-to-horizontal anisotropy in Indonesian oil and gas reservoirs: A general review. SPE. In *SPE international oil conference and exhibition in Mexico*. SPE.103315.

10.1029/2024JB028763

Zhang, S., & Tullis, T. E. (1998). The effect of fault slip on permeability and permeability anisotropy in quartz gouge. *Tectonophysics*, *295*(1–2), 41–52. https://doi.org/10.1016/s0040-1951(98)00114-0

Zhang, S., Tullis, T. E., & Scruggs, V. J. (1999). Permeability anisotropy and pressure dependency of permeability in experimentally sheared gouge materials. *Journal of Structural Geology*, *21*(7), 795–806. https://doi.org/10.1016/s0191-8141(99)00080-2

Zhu, W., Montési, L. G., & Wong, T. F. (2002). Effects of stress on the anisotropic development of permeability during mechanical compaction of porous sandstones. *Geological Society, London, Special Publications*, *200*(1), 119–136. https://doi.org/10.1144/gsl.sp.2001.200.01.08